Article

Fragment Screening Identifies Novel Allosteric Binders and Binding Sites in the VHR (*DUSP3*) Phosphatase

Jiaqian Wu,[#] Marek R. Baranowski,[#] Alexander E. Aleshin, Eta A. Isiorho, Lester J. Lambert, Laurent J. S. De Backer, Ye Na Han, Ranajit Das, Douglas J. Sheffler, Andrey A. Bobkov, Alexis M. Lemberikman, Daniel A. Keedy, Nicholas D. P. Cosford, and Lutz Tautz*

ACCESS | Metrics & More | Article Recommendations | Supporting Information

ABSTRACT: The human *Vaccinia* H1-related phosphatase (VHR; *DUSP3*) is a critical positive regulator of the innate immune response. Recent studies suggest that inhibiting VHR could be beneficial in treating sepsis and septic shock. VHR belongs to the superfamily of protein tyrosine phosphatases (PTPs), a large class of enzymes that are notoriously difficult to target with small molecules. Fragment-based drug discovery (FBDD) has emerged as an effective strategy for generating potent ligands, even for challenging drug targets. Here, we present a fluorine NMR-based discovery platform for identifying fragments that bind to VHR. This platform encompasses automated library assembly, mixture formation, quantitative material transfer, fluorine NMR screening, and biophysical hit confirmation. We demonstrate that this streamlined, integrated screening workflow produces validated hits with diverse chemical matter and tangible structure−activity relationships (SAR). Crystal structures yielded detailed information on the fragment-protein interactions and provide a basis for future structurally enabled ligand optimization. Notably, we discovered novel ligand binding sites on VHR, distant from the conserved active site, facilitating the generation of selective VHR modulators. This fragment discovery platform can be applied to other PTPs and holds significant potential for identifying potent and selective ligands.
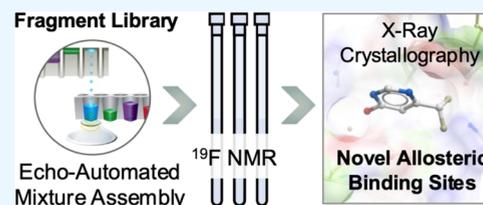
■ INTRODUCTION

Sepsis and septic shock are caused by a dysregulated host immune response to infection, ultimately resulting in tissue damage, organ failure, and often death.[1] Effective treatment options for sepsis and septic shock are limited, and the mortality rate is extremely high with up to 50% for sepsis and up to 80% for septic shock.[2] The dual-specificity phosphatase 3 (DUSP3), also known as *Vaccinia*-H1-related phosphatase (VHR),[3] is a critical regulator of the innate immune response. VHR is highly expressed in human monocytes and macrophages, cells that are responsible for proinflammatory cytokine and chemokine secretion that signal the recruitment and activation of lymphocytes.[4] Genetic reduction of VHR was found to confer strong protection against sepsis and septic shock, suggesting that targeting VHR may provide a novel therapeutic strategy for the treatment of these life-threatening conditions.[4] VHR belongs to the superfamily of protein tyrosine phosphatases (PTPs), important signaling molecules that have been implicated in many diseases.[5−9] A major hurdle in targeting PTPs with small molecules is posed by the highly conserved and highly charged active site. Inhibitors targeting the PTP active site are often potent but lack selectivity and suffer from low cell membrane permeability due to their charged nature.[10−12] Indeed, previously reported VHR active site inhibitors lack sufficient efficacy and/or specificity under physiological conditions (Figure S1).[13−19]

Fragment-based drug discovery (FBDD) has become a powerful complementary approach to traditional high-throughput screening (HTS).[20,21] FBDD is based on the concept that drug-like molecules can be developed from smaller and simpler ligands (fragments), that possess a reduced but specific binding energy.[20] The discovery of such fragments, which typically adhere to the "rule of 3" ("Ro3": molecular weight <300, cLog P ≤3, number of hydrogen bond donors ≤3, number of hydrogen bond acceptors ≤3),[22] is at the core of the FBDD approach. Compared to the screening of drug-like molecules using HTS, FBDD has several advantages: First, due to the lower complexity of fragments, the number of compounds that are typically screened and cover a comparable chemical space is about 3 orders of magnitude lower.[23] Second, owing to their small size and higher probability of matching a target protein binding site, fragments often have very good ligand efficiency (LE), a measure of free energy of binding (ΔG) per heavy atom and an important parameter for lead optimization.[24,25] Third, because fragments typically are highly soluble in aqueous solutions, the success rate of solving X-ray
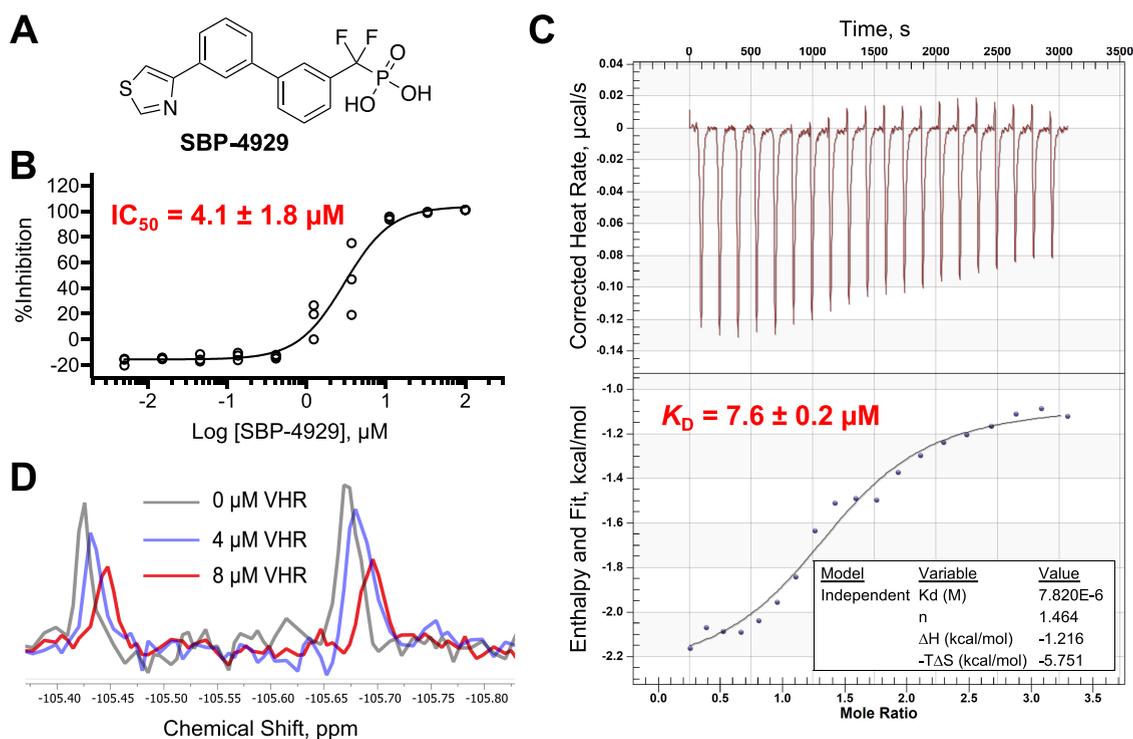
Figure 1. Characterization of fluorine-containing probe compound SBP-4929 and ^{19}F NMR proof-of-concept studies. (A) Chemical structure of VHR probe compound SBP-4929. (B) Dose−response inhibition of VHR by SBP-4929. VHR phosphatase activity was measured using the fluorogenic phosphatase substrate 3-O-methylfluorescein phosphate (OMFP). The IC_{50} value represents the geometrical mean from three independent experiments ± SEM. (C) Isothermal titration calorimetry (ITC) binding experiment of SBP-4929 with VHR. The dissociation constant (K_D) represents the mean of two independent experiments ± SEM. (D) Fluorine NMR spectra were recorded for SBP-4929 (100 μM) at 400 MHz in phosphate-buffered saline (PBS) buffer (pH ∼ 7.4). ^{19}F NMR traces are shown for the SBP-4929 compound in the absence (0 μM) and presence (4 and 8 μM) of VHR.

crystal structures of protein:fragment complexes is typically high, allowing for subsequent rational, structurally enabled chemical optimization.[26] Fourth, starting from hits that comply with the Ro3, optimized leads from fragments are more likely to have properties in the range desired for lead-likeness.[27,28] Last but not least, fragment screening is known to identify novel binding pockets on protein surfaces.[29]

Because fragments naturally have weaker binding affinities than drug-like small molecules, sensitive biophysical screening methods such as NMR[30−33] and X-ray crystallography[34−36] are particularly suitable for the screening of fragment libraries. Among the various NMR methods proposed for compound library screening, ligand-observed fluorine NMR has gained large popularity in drug discovery during the past decade and has become a powerful tool to produce high quality hits.[37,38] Binding of a fluorinated ligand to a target protein typically results in a shift in frequency, or a reduction in peak intensity, of the ligand ^{19}F signal. The high sensitivity of this biophysical assay makes it particularly suitable for identifying fragment hits. Here, we present an FBDD platform for the VHR phosphatase. This workflow includes automated library assembly, mixture formation, quantitative material transfer, fluorine NMR screening, and biophysical hit confirmation. Our streamlined, integrated screening process produced high-quality confirmed hits for subsequent mechanism-of-action (MOA) and structure−activity relationship (SAR) studies. Notably, we discovered several fragments that bind to novel sites on VHR, distant from the conserved active site. Given the challenging nature of phosphatases in drug discovery, our approach holds

promise for identifying progressable fragment entities that could enable the development of highly selective VHR ligands.

■ RESULTS AND DISCUSSION

VHR Protein and Chemical Probe Characterization. NMR screening and biophysical studies require large quantities of highly pure protein. Thus, we established and optimized a bacterial expression system to produce full-length human VHR (24 mg per 1 L cell culture). The enzymatic activity of the recombinant protein was assessed by adapting a standard fluorescence intensity assay using 3-O-methylfluorescein phosphate (OMFP) as the substrate.[39] A Michaelis−Menten kinetics experiment was performed to determine the Michaelis−Menten constant (K_m) for OMFP with VHR (K_m = 5.4 μM). Next, to set up and validate ^{19}F NMR VHR binding experiments, we employed a novel, fluorine-containing VHR chemical probe (SBP-4929, Figure 1A). SBP-4929 contains a difluoro(phenyl)methyl-phosphonate (F_2PMP) group, which is a nonhydrolyzable phosphotyrosine (pTyr) mimetic. F_2PMPs such as SBP-4929 have been previously shown to inhibit the activity of PTPs such as PTP1B by competing with substrate binding at the active site.[40−42] We identified SBP-4929 as a potent VHR orthosteric, active site inhibitor from a series of F_2PMPs we designed, synthesized, and tested against a panel of PTPs (to be published elsewhere). The four-step synthesis of SBP-4929 is shown in Figure S2. In a dose−response VHR inhibition assay using OMFP as the substrate, the IC_{50} value for SBP-4929 was determined to be 4.1 ± 1.8 μM (Figure 1B). Biophysical binding of SBP-4929 to the VHR protein was confirmed using isothermal titration calorimetry
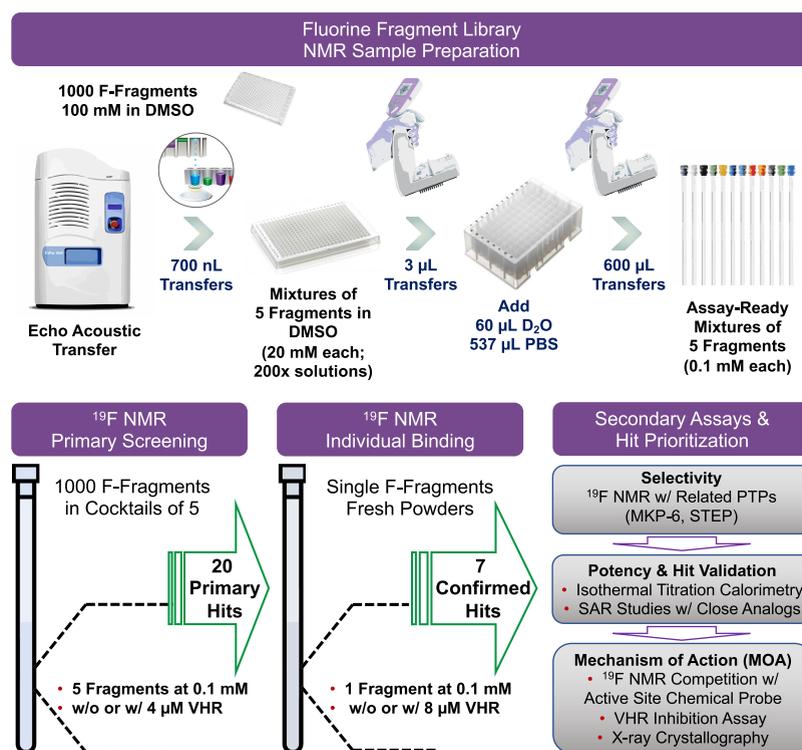
Figure 2. Experimental workflow and data summary from screening of the Enamine fluorinated fragments diversity set library (FDS-1000) using ^{19}F NMR. Upper Panel: A convenient and efficient workflow was developed for NMR sample preparation using Echo acoustic dispensing and multichannel pipet transfers for preparing mixtures of five fragments from library stock solutions. Lower panel: 200 fragment mixtures were screened using ^{19}F NMR. Primary hits were confirmed from fresh powder stock solutions in individual ^{19}F NMR experiments. Secondary assays included experiments to assess the selective binding of fragments to VHR by using ^{19}F NMR assays to counterscreen against two related phosphatases (MAP kinase phosphatase 6, MKP-6, and striatal-enriched protein tyrosine phosphatase, STEP). Further, binding of fragments was characterized and quantified using isothermal titration calorimetry (ITC). Hit scaffolds were validated by testing close analogs to establish an initial structure−active relationship (SAR). The mechanism of action (MOA) of fragments was studied using ^{19}F NMR competition assays employing our active site chemical probe SBP-4929. Detailed information on fragment-VHR binding was gained from X-ray crystallography studies.

(ITC) (Figure 1C). The dissociation constant (K_D) of SBP-4929 for VHR was determined to be 7.6 ± 0.2 μM. Thus, the observed binding affinity of SBP-4929 by ITC matches the measured biochemical assay IC_{50} potency. Next, we set up an ^{19}F NMR experiment to determine if this NMR method can detect binding of SBP-4929 to VHR. As shown in Figure 1D, a distinct doublet signal of ^{19}F was observed for SBP-4929, corresponding to the two fluorine atoms coupled to the phosphorus atom. After addition of 4 or 8 μM VHR, respectively, a combination of dose-dependent changes in the chemical shift, as well as peak intensity reduction of the ^{19}F signals, were observed, indicating binding of SBP-4929 to VHR. The fluorine nucleus is a sensitive measure of chemical environment and transverse relaxation rate. The observed changes in the ^{19}F signals, combined with the measured kinetic potency and biophysical affinity, is indicative of SBP-4929 binding to VHR. Further, we determined the ^{19}F transverse relaxation time T2 for SBP-4929, both in the absence and presence of VHR. The observed faster decay of T2 relaxation with VHR present supports binding of SBP-4929 to VHR (Figure S3).[43,44] Thus, we demonstrated the suitability of SBP-4929 as a probe compound and established a fluorine NMR binding assay for VHR.

^{19}F NMR Fragment Library Screening and Hit Confirmation. To identify fragment binders to VHR, we chose to screen the Enamine fluorinated fragments diversity set (FDS-1000), a commercially available library of 1000 chemi-

cally diverse fluorinated fragments. This well-curated set contains a large variety of chemical scaffolds and excludes trivial cores with overused chemistry, compounds with more than two stereocenters or having rotamers, diastereoisomeric mixtures, as well as molecules prone to aggregation. The library is fully Ro3 compliant and has no reactive compounds. Moreover, the stability of each compound in dimethyl sulfoxide (DMSO) solution has been verified. According to Enamine, each fragment has an experimentally confirmed solubility in PBS buffer at 1 mM, and in DMSO at 200 mM.[45] ^{19}F NMR chemical shifts are provided by Enamine for all compounds in aqueous PBS or DMSO solutions. Of note, Enamine maintains ∼15,000 in-stock analogs, including ∼5400 fluorinated compounds, ranging in molecular weight from 160 to 400. This allows rapid hit validation and initial SAR studies using an analog-by-catalog (ABC) approach.

The FDS-1000 library was acquired in 384-well format compatible with automated liquid handling equipment. We established a workflow in which we used an Echo Acoustic Liquid Handler to efficiently generate mixtures of fragment stock solutions (Figure 2). Based on preliminary experiments, we settled on using mixtures of five fragments for screening. This allowed easy deconvolution of the NMR spectra, while still maintaining sufficient throughput and efficient use of the VHR protein material. Using the Echo liquid handler, 700 nL of each of five consecutive library compounds were transferred into one well of a 384-well PCR plate. In total, 200 wells were

prepared, each containing 3.5 μL of a mixture of five fragments at a concentration of 20 mM per fragment. Additional wells contained SBP-4929 as the positive control. For efficient liquid transfer, NMR assay solutions were prepared in 96-well deep well plates, with each well containing 537 μL PBS buffer and 60 μL D_2O. Fragment mixtures (3 μL each) were transferred to the deep well plate using a multichannel pipet, resulting in a final concentration of 100 μM for each fragment. The assay ready solutions could then be quantitatively transferred to standard NMR tubes using a multichannel pipet, and an ^{19}F NMR spectrum was recorded for each mixture ("unbound spectrum"). Next, recombinant VHR was added (4 μM final), and an ^{19}F NMR spectra was recorded again ("bound spectrum"). The final compound to protein ratio was 25:1. An example of the ^{19}F NMR screening data for one mixture is shown in Figure 3.
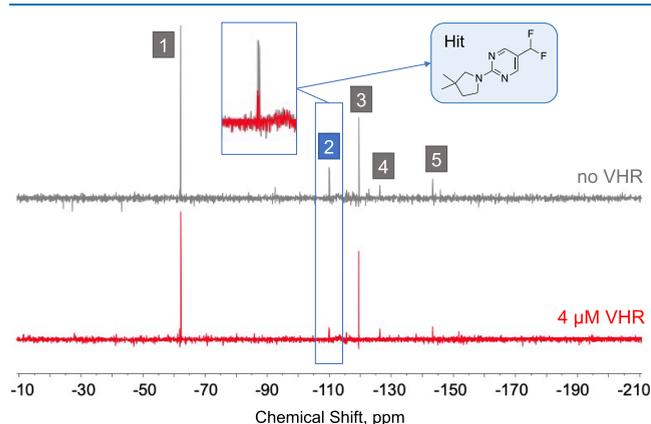

Figure 3. Example data from ^{19}F NMR fragment library screening. ^{19}F NMR data are shown for one mixture of five fragments (labeled 1 through 5) in the absence (gray) or presence (red) of VHR. The peak intensity reduction for fragment 2 in the presence of VHR indicates binding of this fragment to VHR. Hence, fragment 2 is considered a hit. ^{19}F NMR experiments were recorded at 376 MHz using a JEOL 400 MHz instrument at 298 K.

Hit thresholds were defined as follows: Change in the ^{19}F signal chemical shift $(\Delta\delta) \geq 4$ Hz; or ^{19}F peak intensity reduction $\geq 20\%$; or ^{19}F peak width broadening ≥ 3 Hz. Based on these criteria, 20 primary hits were identified from screening the mixtures. For hit confirmation, the primary hits were tested individually from library stock solutions using the ^{19}F NMR assay. Binding for seven of the 20 hits was confirmed, corresponding to a final confirmed hit rate of 0.7%. Next, we obtained all seven confirmed hits as fresh powders, which were quality controlled using standard ^{1}H NMR and liquid chromatography—mass spectrometry (LC-MS) methods. Powders were then retested for binding using a ^{19}F NMR Carr—Purcell—Meiboom—Gill sequence (CPMG) experiment, which enhances line broadening arising from interaction between a ligand and a protein.[37,46] Using this benchmark, binding to VHR for all seven fragments was confirmed from the fresh powder stock solutions. The chemical structures of the seven hits and their ^{19}F NMR VHR binding data are shown in Figure 4. Additionally, we assessed the selectivity of the confirmed hits for VHR by testing them against two related PTPs, the dual-specificity phosphatase MAP kinase phosphatase 6 (MKP-6) and the striatal-enriched protein tyrosine phosphatase (STEP), using a similar ^{19}F NMR assay. Except

for F01, no binding of the fragments to the related phosphatases was detected (Figure S4). Thus, six out of seven identified fragments bound with relative selectivity to VHR. Of note, the 100% hit confirmation rate from fresh, quality-controlled powders observed for the fragment binders was in stark contrast to the low powder confirmation rate typically observed in conventional PTP HTS campaigns that use phosphatase activity assays as a primary readout. Biochemical screening assays suffer from a large false positive rate due to the fact that the catalytic cysteine, common to all PTPs, is extremely reactive (pK_a between 4.5 and 5.5)[47] and is easily oxidized or otherwise modified by trace amounts of impurities often found in library compound collections. In contrast, our data demonstrate that ligand-observed fluorine NMR is an effective method for identifying true PTP hit compounds. Moreover, our compound and liquid handling protocol allows for the efficient screening of libraries containing thousands of fragments.

Fragment Hit Validation and Initial SAR Studies. To validate the identified VHR fragments, we procured and tested several close analogs of the various hit scaffolds. Clustering the powder-confirmed hits by chemical similarity analysis using Extended-Connectivity FingerPrints (ECFPs)[48] and a Tanimoto distance[49] of 0.5 revealed six distinct chemical scaffolds (Figure 5A, left panel). We obtained a total of 14 analogs (Figure 5A, right panel) and tested them individually in ^{19}F NMR experiments. We applied activity thresholds similar to the thresholds we used for hit confirmation. The ^{19}F NMR data for active analogs is shown in Figure 5B. Based on the measured activities, several observations could be made. *Cluster 1:* Analogs F08, F09, and F10, which differ from the parent fragment (F03) by the addition of various *N*-substituents at the pyrimidinedione ring, did not show binding to VHR, suggesting that either the unsubstituted amide nitrogen in the pyrimidinedione ring is important for binding, or that the binding site does not accommodate any larger substituents at this position. *Cluster 2:* Analogs F11 and F12 did not show binding to VHR. Compared to the parent fragment (F02), F11 and F12 do not contain the trifluoromethyl group in the 8-position of the quinazolinone ring, but instead feature 6-methyl and 7-fluoro substituents (F11) or a 5-fluoro substituent (F12), respectively, suggesting that either the trifluoromethyl group in the 8-position is required for binding, or that the additional substituents in 6/7- or 5-position cannot be accommodated by the binding site. *Cluster 3:* All three analogs (F13, F14, and F15) were active. The data suggest that the difluoromethyl group in hit F04 can be replaced with a trifluoromethyl group. Analog F13, containing an additional trifluoromethyl group in 5-position of the benzimidazole ring, was the most potent fragment in this series. *Cluster 4:* Analogs F16, F17, and F18 of the parent fragment F07 were all active. This suggested that the oxoacetic acid in F07 can be replaced with butanoic acid (F16) or acetic acid (F18) without losing activity, and that a benzylamine moiety in F17 can mimic the tetrahydroisoquinoline moiety of the parent compound. *Cluster 5:* Analog F19 appears to be a potent binder. Compared to the parent fragment F05, F19 is lacking the methyl group in the 2-position of the pyrimidine ring and features a difluoromethyl group instead of a trifluoromethyl group in the 6-position. *Cluster 6:* Both analogs F20 and F21 were active. The data suggest that the 3,3-dimethylpyrrolidine moiety (F01) can be replaced with a 5-methyl-3,6-dihydropyridine moiety (F21) without losing activity. Similarly, a triazole ring (F20) is
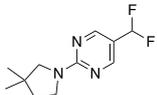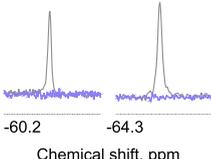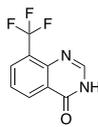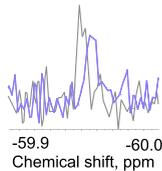
Fragment ID	Chemical Structure	Molecular Weight	^{19}F NMR Spectra (Grey, 0 μM VHR; Blue, 8 μM VHR)	Selective Binding over MKP-6	Selective Binding over STEP$_{46}$
F01		227.26		n/d	No
F02		214.14		Yes	Yes
F03		200.17		Yes	Yes
F04		202.59		Yes	Yes
F05		178.11		Yes	Yes
F06		178.11		Yes	Yes
F07		223.20		Yes	Yes
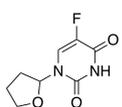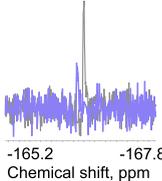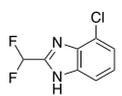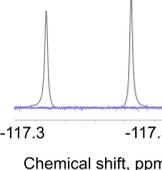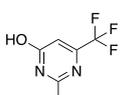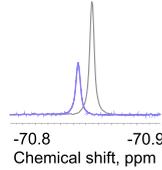
Figure 4. Confirmed VHR hits from screening the Enamine fluorinated fragment library. Shown are the chemical structures of the hits and their ^{19}F NMR signals from fresh powders in the absence (gray) and presence of VHR (8 μM, blue). Changes in the chemical shift or peak intensity indicate binding. A measure of selectivity of fragment hits for VHR was determined by comparison to similar experiments using the related phosphatases MKP-6 and STEP$_{46}$ (see Figure S3 for NMR spectra).

accepted in place of the pyrimidine ring in the parent compound. In summary, the data demonstrate that our fragment screening platform yields hits with diverse chemical matter and a tangible SAR. Notably, our studies with commercially available analogs provided additional activity validation for scaffolds 3, 4, 5, and 6, along with preliminary initial SAR insights.

Mechanism of Action (MOA) Studies. To further investigate the fragment scaffolds, we tested whether the identified hits bind to the active site or a yet undefined, novel binding site in VHR. To assess potential active site interaction,
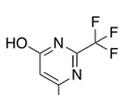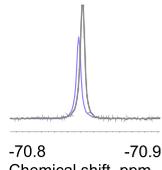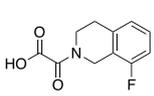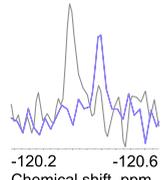
we utilized our fluorine-containing active site probe compound SBP-4929 to set up a ^{19}F NMR competition assay. As shown in Figure 1D, binding to VHR causes a change in the chemical shift and an intensity decrease of the SBP-4929 ^{19}F NMR signal. Fragments that compete with SBP-4929 binding at the VHR active site are expected to revert these changes to match the SBP-4929 ^{19}F NMR chemical shifts and signal intensities measured in the absence of VHR. Using this assay format, we found that most identified hits did not compete with SBP-4929 binding to VHR when using a fragment:SBP-4929 ratio of 10:1 (Figure 6). However, three fragments—F01, F05, and F07—
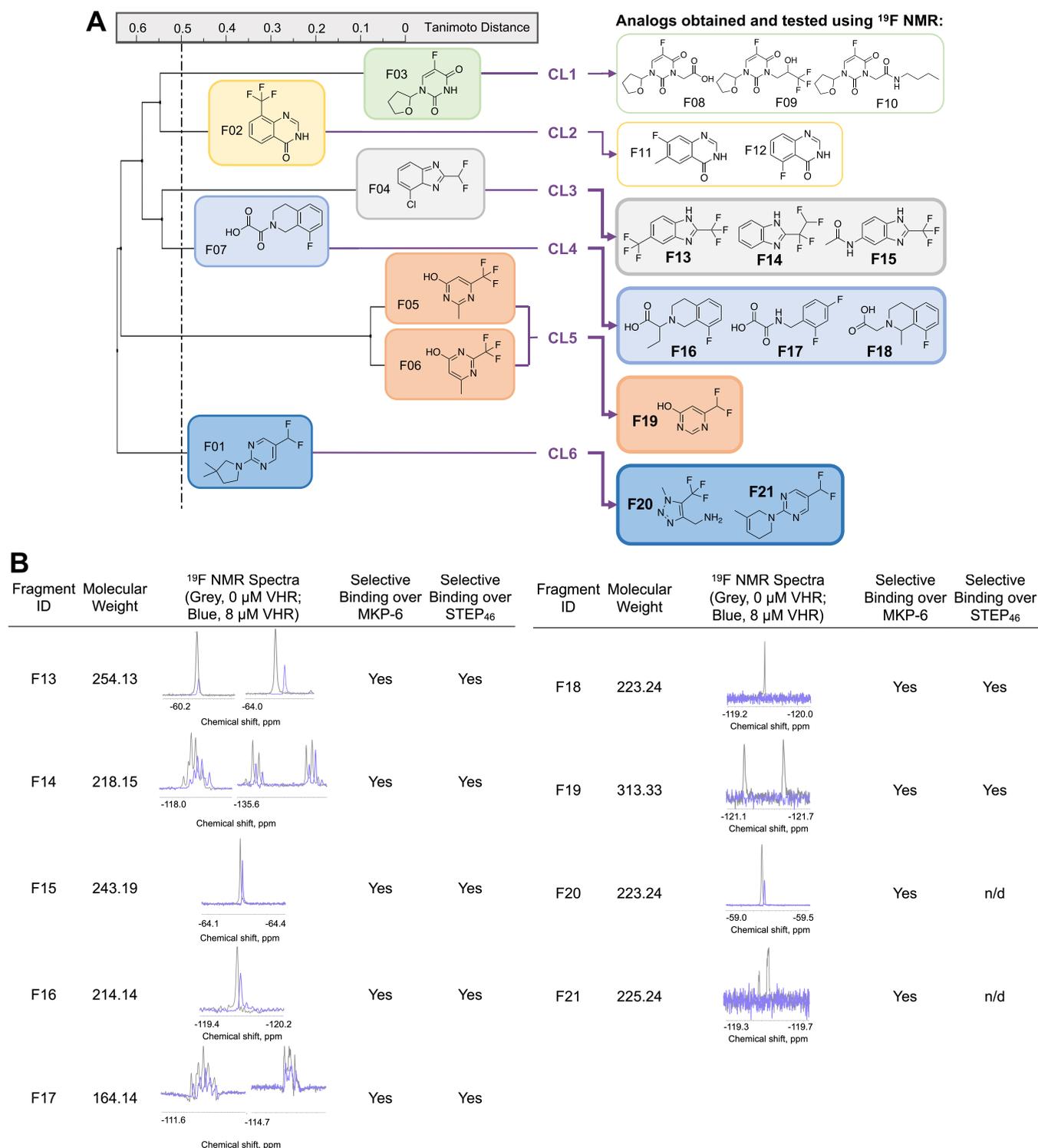
Figure 5. Hit clustering and initial SAR studies. (A) Left panel: Clustering VHR fragment hits by chemical similarity analysis using Extended-Connectivity FingerPrints (ECFPs)[48] and a Tanimoto distance[49] of 0.5 revealed six distinct chemical scaffolds (clusters 1−6, CL1−6). Right panel: Fluorinated analogs for each scaffold were available. A total of 14 analogs were obtained and tested. Active analogs in the ^{19}F NMR binding assay are labeled in bold. (B) ^{19}F NMR data from fresh powders for active analogs. Changes in the ^{19}F signal chemical shift ($\Delta\delta$) or ^{19}F peak intensity reduction between the spectra recorded in the absence (gray) and presence of VHR (blue) indicate binding. The selectivity of fragment analogs for VHR was determined in similar experiments using the related phosphatases MKP-6 and STEP$_{46}$ (see Figure S3 for NMR spectra).

showed partial or complete reversion of the SBP-4929 ^{19}F NMR signal, respectively, suggesting active site binding. To further validate these findings, we tested analogs of F05 and F07 using the same competition assay format. For F07, analog F17 also demonstrated strong competition with SBP-4929

binding (Figure 6). In contrast, for F05, the closely related fragment F06 and analog F19 did not affect SBP-4929 binding to VHR, suggesting that the F05/F06 scaffold does not target the active site. We also employed our established VHR enzymatic assay (using OMFP as the substrate) to test all

Fragment ID	SBP-4929 ^{19}F NMR Spectra*	Intensity Recovery (%)	Chemical Shift Recovery (%)	Competitive Binding**
F01		87	83	yes
F02		0	0	no
F03		0	46	no
F04		12	0	no
F05		67	0	yes
F06		0	0	no
F07		30	0	yes
F17		67	0	yes
F19		0	0	no
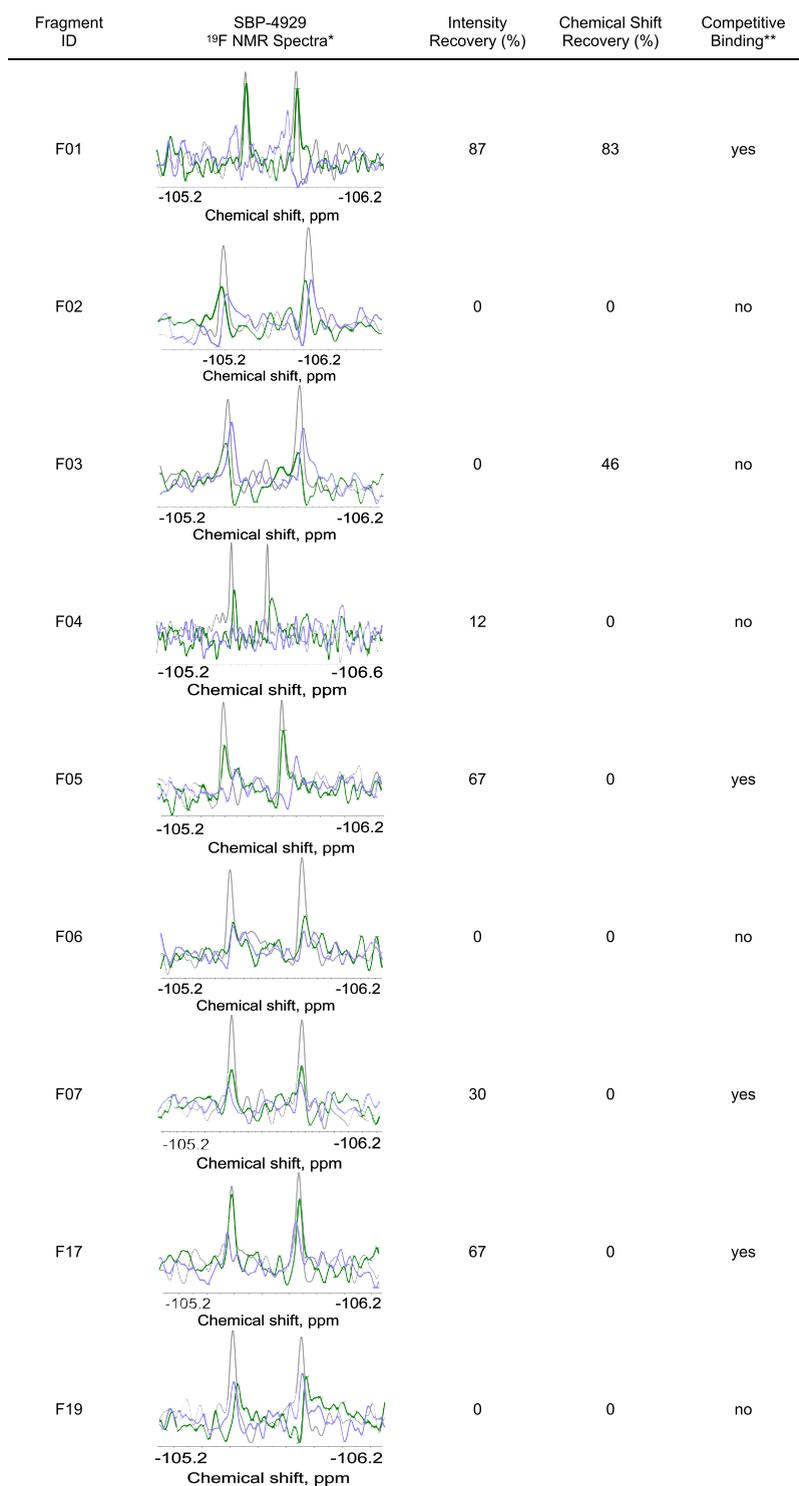
Figure 6. ^{19}F NMR competition assay with active site probe SBP-4929. Fragment hits and selected analogs were tested for their ability to compete with the binding of SBP-4929 (100 μM) at the VHR active site. *Gray, 0 μM VHR; Blue, 8 μM VHR; Green, 8 μM VHR + fragment (1000 μM). **Set threshold for competitive binding: intensity recovery, 30%; chemical shift recovery, 50%.

fragment hits in a 10-point dose−response biochemical inhibition experiment. Only F07 exhibited measurable inhibition at concentrations up to 2.5 mM (IC$_{50}$ = 490 μM), supporting the notion that the F07 scaffold targets the VHR active site. Using ITC, we determined the K_D of F07 for VHR to be 2.0 ± 1.0 mM (Figure S5), consistent with its IC$_{50}$ value. We also measured K_D values for additional fragments, including F07 analogs F17 and F18, and found they bind to

VHR with similar affinities (Figure S5). Collectively, the competition, inhibition, and binding studies demonstrated that our NMR screening platform can identify both active site-binding fragments as well as fragments that bind VHR without inhibiting it.

X-ray Crystallography Studies. Detailed information on the specific interactions between identified fragments and the target protein is invaluable for prioritizing and advancing

Figure 7. X-ray structure of F17 bound to VHR (PDB ID 8TK2). (A) Fragment F17 (pink) bound to the active site in VHR. Hydrogen bonding interactions are indicated with dashed lines. (B, C) Electron density of F17 in the two VHR molecules that are present in the unit cell. The $F_o−F_c$ electron density maps omitting F17 atoms are shown as a blue mesh contoured at $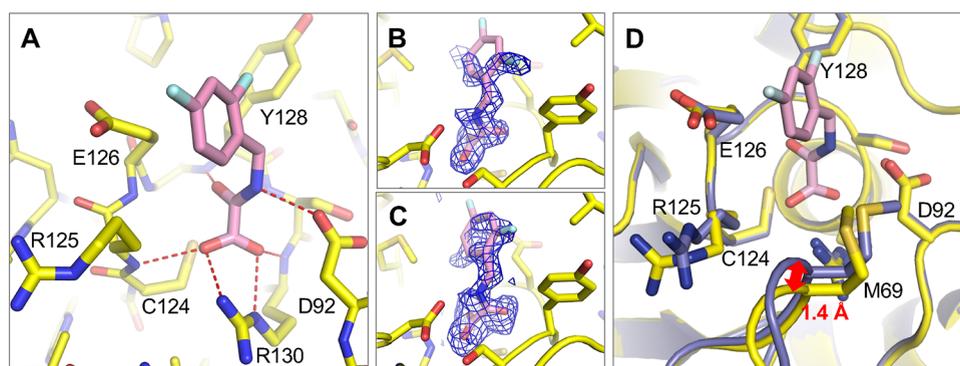3\sigma$ confidence level. (D) Comparison of the active site in the crystal structures of apo-VHR (blue) and VHR bound to F17 (yellow). The loop containing M69 deviates by up to 1.4 Å, presumably to accommodate binding of F17. Similarly, the side chain of R125 undergoes a conformational change, likely induced by binding of F17. The figure was generated using PyMol (v 2.1).

fragment scaffolds. To this end, we employed X-ray crystallography to determine the binding sites of selected fragments through VHR cocrystallization trials and soaking experiments. We successfully solved high-resolution structures for two fragments, F17 and F19, in complex with VHR (Figure 7). Data collection and refinement statistics are provided in Table 1. Additionally, we solved four supplementary crystal structures: (1) apo-VHR form 1 (Figure S6), (2) apo-VHR form 2 (Figure S6), (3) VHR with a phosphate ion bound to the active site (Figure S7), and (4) VHR with a 2-(4-(2-hydroxyethyl)piperazin-1-yl)ethane-1-sulfonic acid (HEPES) molecule bound to the active site (Figure S8). Data collection and refinement statistics for these structures are detailed in Table S1. Notably, all of our crystal structures offer higher resolution than previously reported VHR structures (1VHR.pdb,[50] 1J4X.pdb,[51] and 3F81.pdb[18]). Furthermore, some of our structures exhibited novel crystal packing arrangements, leading to local structural differences in various VHR sites (Figure S9), which may enhance the potential of future soaking experiments to identify novel binding sites for nonactive site binders.

Crystals of the VHR-F17 complex were obtained by cocrystallization using the sitting drop vapor diffusion technique. The VHR-F17 structure was solved by molecular replacement to 1.7 Å resolution, with R and R_{free} factors of 17.6 and 22.3%, respectively. The electron density $F_o−F_c$ omit maps clearly indicated the presence of F17 in the active site of VHR (Figure 7A−C), consistent with results from the ^{19}F NMR competition assay using our active site probe compound SBP-4929 (Figure 6). The oxoacetic acid moiety of F17 formed multiple hydrogen bonds with residues of the phosphate-binding loop (P-loop) in VHR, mimicking the interactions of the natural phosphotyrosine during substrate binding.[51] More specifically, a salt bridge was observed between the oxoacetic acid and the guanidinium group of the invariant arginine (R130) in the PTP signature motif $C(X)_5R$ that forms the P-loop.[47] Additional hydrogen bonds occurred between the oxoacetic acid and the backbone amide nitrogen atoms of R125, Y128, and R130. The amino group of F17 also formed hydrogen bonds with the side chain carboxylic acid of D92, the general catalytic acid−base within the acid loop (WPD-loop).[47] Lastly, the difluorobenzene ring of F17 was stabilized by van der Waals interactions with the side chains of E126 and

Table 1. Data Collection and Refinement Statistics (Molecular Replacement)[a,b]

	VHR-F17 complex (PDB: 8TK2)	VHR-F19 complex (PDB: 8TK3)
data collection		
beamline	SSRL BL12−2	NSLS-II 17-ID-1
space group	P1	P2₁2₁2₁
cell dimensions		
a, b, c (Å)	35.54 44.39 59.86	34.13 52.47 100.49
α, β, γ (deg)	78.1 90.0 81.7	90 90 90
resolution (Å) (outer shell)	38.7−1.70 (1.73−1.70)	50.3−1.95 (2.18−1.95)
no. reflections	34755 (1610)	13585 (3842)
wavelength (Å)	0.97946	0.9201
R_{merge}	0.049 (0.23)	0.13 (0.68)
$I/\sigma I$	8.8 (2.7)	7.8 (2.7)
CC1/2	0.99 (0.65)	0.99 (0.91)
completeness (%)	89.4 (80.9)	99.0 (100.0)
redundancy	2.0 (1.9)	6.4 (7.0)
refinement		
resolution (Å)	38.7−1.7	40.3−2.0
no. reflections/test set	32683/2065	12090/632
R_{work}/R_{free}	0.176/0.223	0.186/0.255
no. atoms		
overall	3211	1581
protein	2930	1443
ligand/ion	41	32
water	240	106
B-factors		
overall	32	34.1
protein	31	32.6
ligand/ion	57.9	73.6
water	39.7	42.9
R.M.S. deviations		
bond lengths (Å)	0.01	0.009
bond angles (deg)	1.47	1.62
Ramachandran favored/outliers (%)	97.2/0.0	95.4/0.0

[a]The data set was collected from a single crystal. [b]Values in parentheses are for the highest-resolution shell.

Y128 in the P-loop. The crystal unit cell contained two VHR molecules, with F17 bound to both, occupying nearly identical
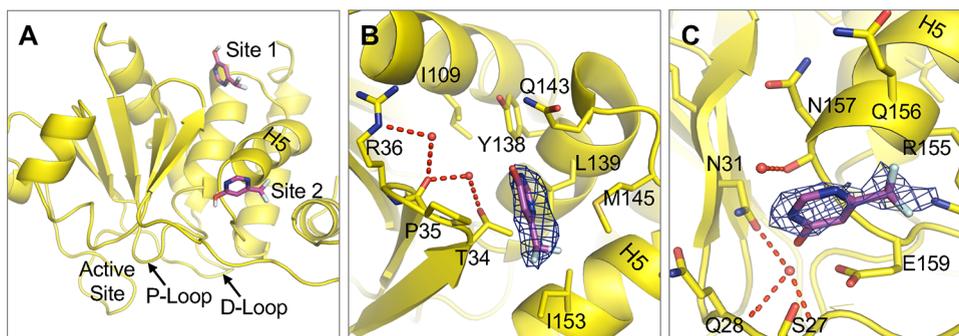
Figure 8. X-ray structure of F19 bound to VHR (PDB ID 8TK3). (A) Fragment F19 (pink) bound to VHR at two sites (site 1 and site 2) that are distinct from the active site. (B) Close-up of F19 bound to site 1 in VHR. F19 (pink) and amino acids that form the binding site are highlighted in stick representation. Two coordinated water molecules within the binding pocket and their hydrogen bonding interactions are highlighted. (C) Close-up of F19 bound to site 2 in VHR. F19 (pink) and amino acids that form the binding site are highlighted in stick representation. Two coordinated water molecules within the binding pocket and their hydrogen bonding interactions are highlighted. In B and C, the F_o-F_c electron density omitting F19 atoms are shown as a blue mesh contoured at 3σ confidence level. The electron density was carved beyond 3 Å distance from the ligand for clarity. The figure was generated using PyMol (v 2.1).

positions with a root-mean-square deviation (r.m.s.d.) of 0.18 Å. Notably, compared to the apo-VHR structure, the loop spanning from A63 to N72 (E-loop)[47] deviated by up to 1.4 Å in the F17-bound structure, likely to accommodate F17 binding (Figure 7D). Additionally, the R125 side chain in the P-loop adopted a different conformation in the VHR-F17 complex compared to apo-VHR, presumably to accommodate the altered E-loop position. Small molecule compounds containing oxoacetic or oxamic acids have been reported as potent inhibitors of other PTPs such as PTP1B and mPTPB.[52−54] Thus, F17 may serve as a valuable starting point for designing potent VHR inhibitors using a structure-guided approach. Notably, VHR P-loop residues R125, E126, and Y128 are unique to VHR among the more than 100 humans PTPs (Figure S9). It may be possible to design analogs of F17 that, in addition to the observed interactions, form specific hydrogen bonds or $\pi-\pi$ interactions with these unique residues in VHR, potentially increasing both the potency and selectivity of VHR inhibitors.

Next, soaking experiments with apo-VHR crystals and various fragments yielded a high-resolution structure of F19 bound to VHR. NMR competition assays with F19 and SBP-4929 indicated that F19 does not bind to the VHR active site (Figure 6). Indeed, in the crystal structure of the VHR-F19 complex, we identified F19 bound to two distinct sites in VHR, both distant from the active site (Figure 8A). The first binding site (site 1) is predominantly hydrophobic, formed by residues T34, P35, Y138, L139, Q143, M145, and I153, with F19 binding primarily via hydrophobic interactions (Figure 8B). The second binding site (site 2) is more polar, involving several backbone carbonyls of helix H5 and the side chains of S27, Q28, N31, R155, and E159 (Figure 8C). At site 2, F19 binding appears to be primarily driven by hydrogen bonding interactions between the hydroxyl group of F19 and the nearby side chains of S27 and E159, as well as the backbone amide nitrogen of E159. Additionally, the two fluorine atoms of F19 are positioned close to the guanidinium group of R155 (3.1 and 3.6 Å, respectively), enabling potential hydrogen bonding interactions. Notably, assignment of the observed electron density to F19 in both binding sites was confirmed by the absence of equivalent electron density in a similarly packed crystal structure of VHR lacking F19 (VHR-PO₄; Table S1). For future structure-based optimization of F19, site 2 may be

more promising due to the multiple hydrogen bonding interactions and the potential for extending F19 into an adjacent pocket occupied by a water molecule. However, site 1 also contains two coordinated water molecules (Figure 8B), offering potential for fragment growing strategies. Notably, no other structures in the Protein Data Bank include ligands F17 or F19. Despite being a commercially available fragment, no binding or potency data for the allosteric binder F19 has been reported in ChEMBL[55] or BindingDB.[56] Combined with our observation that F19 does not bind to the closely related phosphatases MKP-6 and STEP, this fragment presents a strong starting point for developing specific allosteric VHR ligands. In summary, our crystallography studies yielded five high-resolution crystal structures of VHR, including two fragment-VHR complexes. The identified binding sites for F17 and F19 aligned with our ¹⁹F NMR competition assay results, offering detailed insights into fragment-protein interactions and a foundation for future structure-based ligand optimization. Remarkably, F19 was found to bind to two novel small molecule binding sites on VHR, presenting new opportunities for developing allosteric compounds targeting VHR. Additionally, ¹⁹F NMR competition assays with F19 as a probe revealed that fragments F05 and F06 (the parent hits of F19) also competed with F19 for binding, suggesting they bind to one or both of these newly identified sites (Figure S11).

■ CONCLUSIONS

FBDD has proven to be an effective strategy for developing potent ligands, even for challenging drug targets.[57−59] We have developed an NMR-based discovery platform tailored for identifying fragments that bind to VHR, a protein tyrosine phosphatase critical in the innate immune response. This platform is adaptable to other members of the PTP family. Our screening and validation framework leverages ligand-observed fluorine NMR to detect small molecule binding over a broad range of affinities. The sensitivity of ¹⁹F NMR spectroscopy is particularly well suited for VHR, as the fast correlation time of this protein due to its small size (21 kDa) does not favor other relaxation-based techniques such as waterLOGSY and saturation transfer difference (STD) experiments. Additionally, ¹⁹F NMR is efficient in terms of time and data deconvolution. An added advantage is that well characterized hits identified within this NMR assay window, which is a composite of

multiple effects, can be readily adapted into useful tools for further advancement efforts as recently described.[60] Furthermore, we established a robust protocol for generating and screening hundreds of fragment mixtures using semiautomated liquid handling of library stock solutions, utilizing acoustic dispensing via an Echo system, though other liquid handling technologies could also be adapted. To validate this platform, we screened a library of 1000 diverse fragments and identified several selective hits for VHR over two related phosphatases. Additionally, we developed a fluorine-containing active site probe, SBP-4929, which was instrumental in assessing the MOA of hit compounds. Among the hits, we identified fragments that bind to both the active site and, importantly, novel, previously unidentified sites on VHR. Our SAR and X-ray crystallography studies provided detailed insights into the molecular interactions between potent fragments and the VHR protein, forming a foundation for future structure-based optimization. Fragments that bind to novel sites could potentially be optimized into highly effective "warheads" for developing VHR-targeted degraders, such as Proteolysis TArgeting Chimeras (PROTACs). PROTAC technology has recently driven major advancements in drug discovery, enabling selective degradation of previously undruggable targets.[61,62] Unlike inhibitors that target conserved active sites, PROTACs can target any suitable pocket within a protein, facilitating the design of selective degraders based on ligands for nonconserved binding sites.[63] Whether as inhibitors or degraders, selective VHR modulators hold significant therapeutic potential for combating sepsis and septic shock—devastating conditions responsible for nearly 20% of global deaths.[64] Our work establishes a foundation for discovering such therapeutics.

■ EXPERIMENTAL SECTION

Commercial Fragments. The Fluorinated Fragments Diversity Set library (FDS-1000) was obtained from Enamine as 100 mM DMSO stock solutions provided in Labcyte LP-0200 Echo source plates. All fragment hits and analogs were obtained as fresh powders from Enamine and had a purity of >95%.

Chemistry and Synthetic Procedures. All reactions were performed in oven-dried glassware under an atmosphere of nitrogen with magnetic stirring. All solvents and chemicals used were purchased from Sigma-Aldrich or Acros and were used as received. Purity (>95%) and characterization of compounds were established by a combination of liquid chromatography−mass spectroscopy (LC-MS) and NMR analytical techniques for all tested compounds. Silica gel column chromatography was carried out using prepacked silica cartridges from RediSep (ISCO Ltd.) and eluted using an Isco Companion system. ^{1}H, ^{13}C, and ^{19}F-NMR spectra were obtained on a JEOL 400 spectrometer at 400, 101, and 376 MHz, respectively. Chemical shifts are reported in δ (ppm) relative to residual solvent peaks or TMS as internal standards. J-coupling constants are reported in Hz. High-resolution ESI-TOF mass spectra were acquired with an Agilent 6230 TOF LC/MS at the Mass Spectrometry Core at Scripps Research. HPLC-MS analyses were performed on a Shimadzu 2010EV LC-MS using the following conditions: Kromisil C18 column (reverse phase, 4.6 mm × 50 mm); a linear gradient from 10% acetonitrile and 90% water to 95% acetonitrile and 5% water over 4.5 min; flow rate of 1 mL/min; UV photodiode array detection from 200 to 400 nm.

Synthesis of SBP-4929. *Step 1:4-(3-Bromophenyl)-thiazole.* 4-Bromothiazole (1 g, 6.1 mmol), (3-bromophenyl)-boronic acid (1.47 g, 7.4 mmol), and K$_2$CO$_3$ (1.7 g, 12.3 mmol) were mixed with 40 mL of dioxane and 10 mL of water in a round-bottom flask with a stirring bar. Nitrogen was bubbled through the mixture for 15 min while stirring. Pd(PPh$_3$)$_4$ (709 mg, 0.6 mmol) was added under nitrogen and the mixture was refluxed under nitrogen for 16 h, then cooled down to room temperature and extracted with EtOAc, dried over sodium sulfate, and purified by column chromatography on silica gel using hexane/EtOAc (100:0 to 50:50) as eluting solvents. 680 mg of the product was obtained (yield: 47%). LC-MS observed [M + H]$^+$: 242.06. ^{1}H NMR (400 MHz, CDCl$_3$-d) δ 7.29 (s, 0H), 7.41−7.47 (m, 1H), 7.52 (d, J = 1.8 Hz, 1H), 7.81 (dt, J = 7.8, 1.4 Hz, 1H), 8.07 (t, J = 1.8 Hz, 1H), 8.84 (d, J = 1.8 Hz, 1H). ^{13}C NMR (101 MHz, CDCl$_3$-d) δ 113.72, 123.09, 125.05, 129.62, 130.45, 131.27, 136.23, 153.23, 154.89.

Step 2: (3′-(Thiazol-4-yl)-[1,1′-biphenyl]-3-yl)boronic Acid. 4-(3-Bromophenyl)thiazole (600 mg, 2.6 mmol), 1,3-phenylenediboronic acid (834 mg, 5.2 mmol), and K$_2$CO$_3$ (674 mg, 5.2 mmol) were mixed with 40 mL of dioxane and 10 mL of water in a round-bottom flask with a stirring bar. Nitrogen was bubbled through the mixture for 15 min while stirring. Pd(PPh$_3$)$_4$ (290 mg, 0.26 mmol) was added under nitrogen and the mixture was refluxed under nitrogen for 16 h, then cooled down to room temperature, extracted with EtOAc, dried over sodium sulfate, and purified by column chromatography on silica gel using dichloromethane/methanol (100:0 to 90:10) as eluting solvents. 240 mg of the product was obtained (yield: 34%). LC-MS observed [M + H]$^+$: 282.20. ^{1}H NMR (400 MHz, CDCl$_3$-d) δ 8.79 (d, J = 2.3 Hz, 1H), 8.10 (d, J = 2.3 Hz, 1H), 8.06 (d, J = 2.3 Hz, 1H), 7.85−7.83 (m, 2H), 7.75−7.73 (m, 1H), 7.48−7.41 (m, 4H), 4.19 (q, J = 7.3 Hz, 4H), 1.30 (t, J = 7.3 Hz, 6H). ^{13}C NMR (101 MHz, CDCl$_3$-d) δ 206.80, 153.30, 153.11, 142.78, 141.67, 138.29, 135.00, 131.51, 129.60, 129.34, 129.02, 128.88, 127.29, 125.98, 125.56, 113.22, 64.67, 64.61, 16.56, 16.51.

Step 3: (Difluoro(3′-(thiazol-4-yl)-[1,1′-biphenyl]-3-yl)-methyl)phosphonate. (3′-(Thiazol-4-yl)-[1,1′-biphenyl]-3-yl)boronic acid (100 mg, 0.36 mmol), diethyl (bromodifluoromethyl)phosphonate (189 mg, 0.72 mmol), Xantphos (41 mg, 0.07 mmol) and K$_2$CO$_3$ (98 mg, 0.72 mmol) were mixed with 10 mL of anhydrous dioxane in a round-bottom flask with a stirring bar. Nitrogen was bubbled through the mixture for 15 min while stirring. PdCl$_2$(PPh$_3$)$_2$ (25 mg, 0.07 mmol) was added under nitrogen and the mixture was refluxed under nitrogen for 16 h, then cooled down to room temperature, extracted with dichloromethane, dried over sodium sulfate, and purified by column chromatography on silica gel using hexane/EtOAc (100:0 to 50:50) as eluting solvents. 50 mg of the product was obtained (yield: 15%). LC-MS observed [M + H]$^+$: 424.27. ^{1}H NMR (400 MHz, CDCl$_3$-d) δ 8.79 (d, J = 2.3 Hz, 1H), 8.10 (d, J = 2.3 Hz, 1H), 8.06 (d, J = 2.3 Hz, 1H), 7.85−7.83 (m, 2H), 7.75−7.73 (m, 1H), 7.48−7.41 (m, 4H), 4.19 (q, J = 7.3 Hz, 4H), 1.30 (t, J = 7.3 Hz, 6H). ^{13}C NMR (101 MHz, CDCl$_3$-d) δ 206.77, 153.27, 153.08, 142.75, 141.50, 138.23, 132.47, 131.47, 130.59, 129.95, 127.26, 127.02, 124.92, 120.78, 115.33, 113.19, 62.72, 62.00, 16.51, 16.56.

Step 4: (Difluoro(3′-(thiazol-4-yl)-[1,1′-biphenyl]-3-yl)-methyl)phosphonic Acid (SBP-4929). Diethyl (difluoro-(thiazol-4-yl)-[1,1′-biphenyl]-3-yl)methyl)phosphonate (45

mg, 0.1 mmol) was dissolved in 2 mL of anhydrous CH_3CN; bromotrimethylsilane (49 mg, 0.3 mmol) was added, and the mixture was stirred at 70 °C for 2 h, then cooled down to room temperature and solvent removed under vacuum. The residue was purified by column chromatography on silica gel using dichloromethane/methanol (100:0 to 90:10) as eluting solvents. Fifteen mg of the product was obtained (yield: 41%). LC-MS observed $[M + H]^+$: 368.25. ESI HRMS expected $[M + H]^+$ 368.032730, observed 368.0315. ^1H NMR (400 MHz, DMSO-d_6) δ 9.22 (d, J = 1.9 Hz, 1H), 8.31 (d, J = 1.9 Hz, 1H), 8.26 (d, J = 1.9 Hz, 1H), 8.00 (dd, J = 7.5, 1.6 Hz, 1H), 7.85 (s, 1H), 7.72 (d, J = 7.5 Hz, 1H), 7.65−7.44 (m, 4H), 2.50 (q, J = 1.8 Hz, 3H). ^{13}C NMR (101 MHz, DMSO-d_6) δ 206.95, 155.41, 155.15, 141.34, 139.69, 135.23, 130.06, 128.60, 127.52, 127.06, 126.04, 125.78, 125.26, 124.96, 115.33.

Expression and Purification of Human VHR, STEP$_{46}$, and MKP-6. All reagents and buffers were from Sigma-Aldrich unless stated otherwise. Full-length human VHR (amino acids 1−185) was subcloned from our pGEX-VHR plasmid[18] into the pET-15b expression vector and expressed as N-His8-tagged fusion protein. Transformed BL21 (DE3) *Escherichia coli* cells were grown in LB medium with Kanamycin (75 μg/mL) at 37 °C until the OD$_{600}$ reached approximately 0.8, and VHR expression was induced with 0.7 mM isopropyl-β-D-thiogalactoside (IPTG) for 12 h at 24 °C. Cells were harvested by centrifugation at 3000g for 15 min at 4 °C, resuspended in lysis buffer (30 mM Tris pH 7.5, 300 mM NaCl, 75 mM imidazole, 10% glycerol), and lysed with two passages using an EmulsiFlex-C3 microfluidizer (Avestin Inc., Ottawa, Canada). The lysate was clarified by centrifugation at 15,000g for 50 min and applied to a HiTrap Ni-NTA resin column. The column was washed with lysis buffer, and the VHR protein was eluted with elution buffer (30 mM Tris pH 8.0, 300 mM NaCl, 300 mM imidazole, 10% glycerol). The purity of the VHR protein was confirmed by sodium dodecyl sulfate polyacrylamide gel electrophoresis (SDS-PAGE) gel electrophoresis, and the fractions containing His8-VHR were pooled together, followed by dialysis for 4 h in 50 mM Tris pH 7.0, 200 mM NaCl, 0.1 mM ethylenediaminetetraacetic acid (EDTA), and a second dialysis overnight in 50 mM Tris pH 7.0, 200 mM NaCl, 10 mM dithiothreitol (DTT). The VHR protein was concentrated by ultrafiltration to a final concentration of 157 μM (extinction coefficient used ε_{280} = 10,680 M^{-1} cm^{-1}) and stored at −80 °C.

For X-ray crystallography studies, the N-terminal His-tag was cleaved off using thrombin during dialysis with Tris buffer (20 mM, pH 8). The protein to thrombin ratio was 10 mg per unit of thrombin. After digestion, tag-free VHR protein was purified by incubation with benzamidine sepharose beads (100 μL, Cytiva) and Ni-NTA agarose beads (100 μL, Thermo-Fisher) for 1 h at room temperature to remove thrombin and uncleaved His-VHR, respectively. Beads were spun down, and the supernatant was further purified by size exclusion chromatography using a HiLoad Superdex 200 16/600 column equilibrated with 50 mM Tris pH 8.5 containing 1 mM tris(2-carboxyethyl)phosphine (TCEP) and 0.5 mM EDTA. The collected VHR fractions were supplemented with 10 mM TCEP and stored on ice for immediate use in the crystallization studies.

Human full-length STEP$_{46}$ was expressed and purified as previously reported.[39,65] Human full-length MKP-6 was cloned into pGEX vector and was expressed as N-GST-tagged fusion protein with a thrombin cleavage site between GST and MKP-6. The fusion protein was expressed in BL21(DE3) using a similar protocol as described for VHR above, using ampicillin (100 μg/mL) instead of kanamycin. For MKP-6 purification, the clarified cell lysate in lysis buffer (30 mM Tris pH 7.5, 300 mM NaCl, 10% glycerol) was loaded onto an immobilized glutathione Sepharose column (Cytiva). The loaded column was washed with lysis buffer three times, and the MKP-6 protein was eluted with elution buffer (30 mM Tris pH 7.5, 300 mM NaCl, 10% glycerol, 10 mM reduced glutathione) and then dialyzed against lysis buffer overnight. The dialyzed fusion protein was digested with thrombin (one unit of thrombin for 10 mg of protein) for 1 h at room temperature. After digestion, tag-free MKP-6 protein was purified by incubation with benzamidine Sepharose beads (Cytiva) and glutathione Sepharose beads (Cytiva) for 1 h at room temperature to remove thrombin, GST, and uncleaved GST-MKP-6. Beads were spun down, and the supernatant was further purified using size exclusion chromatography as described for VHR above. The protein was stored at −80 °C at a concentration of 85 μM.

VHR Enzymatic Activity and Michaelis−Menten Kinetic Assays. The enzymatic activity of VHR was tested at room temperature using a standard 384-well format phosphatase fluorescence intensity assay using OMFP (Sigma-Aldrich) as the substrate.[39] The total reaction volume was 25 μL. For enzyme titration assays, 1.25× VHR working solutions were prepared in 50 mM Bis-tris pH 6, 50 mM NaCl, 0.5 mM EDTA, 5 mM DTT and 0.01% Tween-20. Substrate working solution at 5× was prepared for a final concentration of 50 μM in 50 mM Bis-tris pH 6, 50 mM NaCl, 0.5 mM EDTA and 0.01% Tween-20. For each VHR concentration, 20 μL VHR working solution was dispensed in triplicate into a standard volume, flat bottom, black 384-well plate (Greiner FLUOTRAC 200) and incubated at room temperature for 20 min. The VHR reaction was initiated by adding 5 μL of OMFP working solution. The fluorescence intensity was measured for 10 min in kinetic mode using a Tecan Spark multimode microplate reader with an excitation wavelength of 485 nm and an emission wavelength of 535 nm. Initial velocities (V) were determined from the slopes of the progression curve within the linear of the reaction. Nonenzymatic hydrolysis of the substrates (background control) was measured in the absence of VHR protein. Similarly, Michaelis−Menten kinetic assays were performed, in which the substrate was titrated at a fixed VHR concentration (2.5 nM). The Michaelis−Menten constant (K_M) for OMFP with VHR was determined from the initial velocities using the Michaelis−Menten equation and the program GraphPad Prism (version 9) as described.[39]

^{19}F-NMR Fragment Screening and Hit Confirmation. The Enamine fluorinated fragments diversity set (FDS-1000) was purchased from Enamine (Kyiv, Ukraine). Fragments were provided as 100 mM DMSO stock solutions deposited in Echo Qualified Low Dead Volume (LDV) 384-well microplates. Compounds were spotted into 384-well PCR plates (Armadillo #AB-3384) as mixtures of five fragments at 700 nL each using an Echo 555 liquid handler (Labcyte, Beckman Coulter Life Sciences). PCR plates were sealed and stored in a desiccator at room temperature until further use. Using a multichannel pipet, 3 μL of each mixture was transferred to 96-well deep well plate wells (Rainin #17012624) containing 537 μL PBS buffer and 60 μL D$_2$O. Thus, the final concentration of each fragment was 0.1 mM. Using a multichannel pipet, the mixtures were transferred to standard NMR tubes, and ^{19}F

NMR spectra were recorded at 20 °C using a JEOL 400 MHz spectrometer operating at a ^{19}F frequency of 376 MHz. Typical experimental parameters were as follows: ^{19}F excitation pulse, 7 μs; relaxation delay (d1), 2 s; offset, −110 ppm; spectral width, 200 ppm; number of scans, 128. Next, 16 μL of VHR stock solution (157 μM) was added to each NMR tube, and ^{19}F NMR spectra were recorded again. The ^{19}F NMR spectra with and without VHR were compared, and changes in chemical shifts as well as peak intensities were analyzed using the MestReNova software (Mestrelab Research, version 12 or higher). Primary hits were confirmed by testing them individually from library stock solutions using similar conditions as for the screening. Confirmed hits were repurchased as powders. Fresh stock solutions were prepared (100 mM in DMSO-d_6), and hits were retested individually using the ^{19}F CPMG NMR assay and VHR concentrations of 8 μM. Relaxation delay (D1; 10 s); T2 filter (delay list, 0.4 s); delay between refocusing pulse (Tau step, 20 ms). For ^{19}F-NMR competition assays, ^{19}F CPMG NMR spectra were recorded as described above. The VHR protein concentration was 8 μM; SBP-4929 concentration was 200 μM, candidate fragment concentration was 2000 μM.

VHR Inhibition Assays. For 10-point dose−response inhibition assays (final compound concentration ranging from 100 μM to 5 nM), candidate compounds or DMSO (vehicle control) were spotted in triplicate into 384-well assay plates (Greiner FLUOTRAC 200) using an Echo 555 liquid handler (250 nL). VHR and OMFP working solutions were prepared as described above for final concentrations of 2.5 nM VHR and 6 μM OMFP, respectively. VHR working solution (20 μL) or enzyme buffer (20 μL, background control) were dispensed into compound or control wells, respectively, using a Multidrop Combi reagent dispenser (ThermoFisher). The plate was covered and incubated for 20 min at room temperature. The VHR reaction was initiated by the addition of 5 μL OMFP working solution using a Multidrop Combi, and fluorescence intensity was measured for 10 min in kinetic mode using a Tecan Spark multimode microplate reader with an excitation wavelength of 485 nm, and an emission wavelength of 535 nm. The initial velocities were determined from the slopes of the linear progression curves of the VHR reaction. Rates were normalized using the no-enzyme and vehicle controls and analyzed using a nonlinear regression dose−response inhibition model (log inhibitor vs response, variable slope, four parameters) and the program GraphPad Prism (version 9) to obtain IC_{50} values.

Isothermal Titration Calorimetry (ITC). ITC was performed by the Sanford Burnham Prebys Protein Production and Analysis Facility. Using a low-volume Affinity ITC calorimeter (TA Instruments), candidate compound aliquots (6 μL) in PBS containing 5% DMSO at concentrations varying between 0.3 to 5 mM were injected into the calorimeter cell (20 injections). VHR protein concentration in PBS containing 5% DMSO was between 60 and 285 μM. The experiments were performed at 25 °C. Baseline control data were collected from injecting the compound into the cell containing buffer only. ITC data were analyzed using the NanoAnalyze software (TA Instruments).

X-ray Crystallography Studies. Selected fragments were subjected to VHR cocrystallization trials and soaking experiments. For cocrystallization, VHR protein (7 mg/mL) in 50 mM Tris-HCl pH 8.5 containing 1 mM TCEP and 0.5 mM EDTA was mixed at a 1-to-1 ratio with compound (25 mM) in

10% DMSO, 50 mM Tris-HCl pH 8.5, 1 mM TCEP, 0.5 mM EDTA and concentrated 2-fold using a Centricon concentrator (Millipore) with 10 kDa cutoff. The concentrated VHR-compound solution (0.2−0.3 μL) was mixed with 0.2 μL of precipitant solution [100 mM Bis-Tris pH 6.5, 50 mM NH_4F, 28% (w/v) polyethylene glycol monomethyl ether 2000 (PEGME-2000)] and equilibrated at room temperature in a sitting drop plate with 50 μL of the precipitant solution. Crystals appeared within 24 h and grew for additional 1−5 days, before they were flash-frozen in liquid nitrogen. For overnight soaking experiments, apo-crystals obtained using similar conditions as described above were soaked with 25 mM of candidate compound in 100 mM Bis-Tris pH 6.5, 50 mM NH_4F, 28% (w/v) PEGME-2000, 10% (v/v) DMSO for 15 h. VHR crystals with bound phosphate were obtained by cocrystallization. The protein was mixed with the precipitant solution (0.1 M sodium potassium phosphate pH 7.0, 28% w/v PEG 3350) and equilibrated in a 96-well sitting drop plate (Art Robbins Inc.) with 50 μL of the precipitant solution at room temperature. VHR crystals with bound HEPES were obtained by cocrystallization. The protein was mixed with the precipitant solution (100 mM HEPES pH 7.5, 50 mM PEG 4000) and equilibrated in a 96-well sitting drop plate (Art Robbins Inc.) with 50 μL of the precipitant solution at room temperature. Crystals of apo-VHR form 1 were obtained by mixing the protein with the precipitant solution (100 mM Bis-Tris pH 6.5, 50 mM NH_4F, 28% (w/v) PEG-4000) and equilibrated in a 96-well sitting drop plate (Art Robbins Inc.) with 50 μL of the precipitant solution at room temperature. Crystals of apo-VHR form 2 were obtained by mixing the protein at a 2-to-1 ratio with the precipitant solution (100 mM Bis-Tris pH 6.5, 50 mM NH_4F, 26.73% (w/v) PEG-4000) in a 200 nL drop and equilibrating in a 96-well sitting drop plate (Swissci) with 40 μL of the precipitant solution at room temperature. The data sets for apo-VHR form 1 and apo-VHR form 2 (see Table S1) were obtained either from cocrystallization with F04 or from apo crystals soaked with F05, respectively; these compounds were not evident in the final electron density. All crystals grew for 1−5 days and were flash-frozen in liquid nitrogen. X-ray data were collected either at the Stanford Synchrotron Radiation Lightsource (SSRL; beamline BL12−2) or the Brookhaven National Synchrotron Light Source II (NSLS-II; beamlines 17-ID-1 (AMX) and 19-ID (NYX)). The data were collected at wavelengths of 0.97946 and 0.920 Å, respectively (see Tables 1 and S1 for details) at a temperature of 100 K, then processed using the CCP4 software suite[66] or autoPROC.[67] Crystal structures of apo-VHR and VHR complexes were solved by molecular replacement using a previously published VHR structure (PDB code 1VHR; 100% identity) and refined by Refmac5[68] or Phenix.[69] The structures were evaluated and manually corrected in Coot.[70] After refinement, MolProbity[71] and the Protein Data Bank (PDB) validation server were used for structure validation. The obtained crystal structures had space groups $P1$, $P2_1$, or $P2_12_12_1$ with either a single VHR molecule or noncrystallographic dimer in the unit cell. The data collection and refinement statistics are presented in Tables 1 and S1. The structure coordinates were deposited to the Protein Data Bank (PDB) with the accession codes 8TK2, 8TK3, 8TK4, 8TK5, 8TK6, and 9DJ9.

■ ASSOCIATED CONTENT

ⓢ Supporting Information

Reported VHR inhibitors (Figure S1); synthetic scheme for VHR probe compound SBP-4929 (Figure S2); ^{19}F CPMG NMR T2 measurement for SBP-4929 (Figure S3); fragment ^{19}F NMR binding data with STEP and MKP-6 (Figure S4); isothermal titration calorimetry (ITC) data for selected fragments (Figure S5); crystal structures of apo-VHR (PDB IDs 8TK6 and 9DJ9) (Figure S6); crystal structure of the VHR:phosphate complex (PDB ID 8TK4) (Figure S7); crystal structure of VHR in complex with 4-(2-hydroxyethyl)-1-piperazineethanesulfonic acid (HEPES; PDB ID 8TK5) (Figure S8); superposition of all crystal structures of VHR reported in this study (Figure S9); sequence alignment of phosphate-binding loop (P-loop) amino acid residues for all 104 human PTPs (Figure S10); ^{19}F NMR competition assay with nonactive site fragment F19 (Figure S11); data collection and refinement statistics (molecular replacement) for additional VHR high resolution structures (Table S1); ^{1}H and ^{13}C NMR spectra of VHR probe compound SBP-4929; HPLC trace of VHR probe compound SBP-4929; HPLC traces of commercial fragment powders from Enamine (PDF)

Accession Codes

PDB ID Codes: PDB ID 8TK2: Crystal structure of the VHR:F17 complex; PDB ID 8TK3: Crystal structure of the VHR:F19 complex; PDB ID 8TK4: Crystal structure of the VHR:phosphate complex; PDB ID 8TK5: Crystal structure of VHR in complex with HEPES; PDB ID 8TK6: Crystal structure of apo-VHR, form 1; PDB ID 9DJ9: Crystal structure of apo-VHR, form 2. Authors will release the atomic coordinates and experimental data upon article publication.

■ AUTHOR INFORMATION

Corresponding Author

Lutz Tautz − Cancer Molecular Therapeutics Program, NCI-Designated Cancer Center, Sanford Burnham Prebys Medical Discovery Institute, La Jolla, California 92037, United States; ⓞ orcid.org/0000-0002-4075-6238; Email: tautz@sbpdiscovery.org

Authors

Jiaqian Wu − Cancer Molecular Therapeutics Program, NCI-Designated Cancer Center, Sanford Burnham Prebys Medical Discovery Institute, La Jolla, California 92037, United States; ⓞ orcid.org/0009-0004-5987-886X

Marek R. Baranowski − Cancer Molecular Therapeutics Program, NCI-Designated Cancer Center, Sanford Burnham Prebys Medical Discovery Institute, La Jolla, California 92037, United States; Division of Biophysics, Institute of Experimental Physics, Faculty of Physics, University of Warsaw, 02-093 Warsaw, Poland

Alexander E. Aleshin − Cancer Molecular Therapeutics Program, NCI-Designated Cancer Center, Sanford Burnham Prebys Medical Discovery Institute, La Jolla, California 92037, United States

Eta A. Isiorho − Structural Biology Initiative, CUNY Advanced Science Research Center, New York, New York 10016, United States

Lester J. Lambert − Cancer Molecular Therapeutics Program, NCI-Designated Cancer Center, Sanford Burnham Prebys Medical Discovery Institute, La Jolla, California 92037, United States

Laurent J. S. De Backer − Cancer Molecular Therapeutics Program, NCI-Designated Cancer Center, Sanford Burnham Prebys Medical Discovery Institute, La Jolla, California 92037, United States

Ye Na Han − Cancer Molecular Therapeutics Program, NCI-Designated Cancer Center, Sanford Burnham Prebys Medical Discovery Institute, La Jolla, California 92037, United States

Ranajit Das − Cancer Molecular Therapeutics Program, NCI-Designated Cancer Center, Sanford Burnham Prebys Medical Discovery Institute, La Jolla, California 92037, United States

Douglas J. Sheffler − Cancer Molecular Therapeutics Program, NCI-Designated Cancer Center, Sanford Burnham Prebys Medical Discovery Institute, La Jolla, California 92037, United States

Andrey A. Bobkov − Cancer Molecular Therapeutics Program, NCI-Designated Cancer Center, Sanford Burnham Prebys Medical Discovery Institute, La Jolla, California 92037, United States

Alexis M. Lemberikman − Structural Biology Initiative, CUNY Advanced Science Research Center, New York, New York 10016, United States; ⓞ orcid.org/0009-0006-5256-9428

Daniel A. Keedy − Structural Biology Initiative, CUNY Advanced Science Research Center, New York, New York 10016, United States; Department of Chemistry and Biochemistry, City College of New York, New York, New York 10031, United States; PhD Programs in Biochemistry, Biology, and Chemistry, CUNY Graduate Center, New York, New York 10016, United States

Nicholas D. P. Cosford − Cancer Molecular Therapeutics Program, NCI-Designated Cancer Center, Sanford Burnham Prebys Medical Discovery Institute, La Jolla, California 92037, United States; ⓞ orcid.org/0000-0001-7228-4709

Complete contact information is available at:
https://pubs.acs.org/10.1021/acsomega.4c10321

Author Contributions

#J.W. and M.R.B. contributed equally to this paper.

Notes

The authors declare no competing financial interest.

■ ACKNOWLEDGMENTS

■ REFERENCES

(1) Cohen, J. The immunopathogenesis of sepsis. Nature 2002, 420 (6917), 885−891.

(2) Jawad, I.; Luksic, I.; Rafnsson, S. B. Assessing available information on the burden of sepsis: global estimates of incidence, prevalence and mortality. J. Global Health 2012, 2 (1), No. 010404.

(3) Pavic, K.; Duan, G.; Kohn, M. VHR/DUSP3 phosphatase: Structure, function and regulation. *FEBS J.* **2015**, *282* (10), 1871−1890.

(4) Singh, P.; Dejager, L.; Amand, M.; Theatre, E.; Vandereyken, M.; Zurashvili, T.; Singh, M.; Mack, M.; Timmermans, S.; Musumeci, L.; et al. DUSP3 Genetic Deletion Confers M2-like Macrophage-Dependent Tolerance to Septic Shock. *J. Immunol.* **2015**, *194* (10), 4951−4962.

(5) Alonso, A.; Sasin, J.; Bottini, N.; Friedberg, I.; Friedberg, I.; Osterman, A.; Godzik, A.; Hunter, T.; Dixon, J.; Mustelin, T. Protein tyrosine phosphatases in the human genome. *Cell* **2004**, *117* (6), 699−711.

(6) Tonks, N. K. Protein tyrosine phosphatases–from housekeeping enzymes to master regulators of signal transduction. *FEBS J.* **2013**, *280* (2), 346−378.

(7) Tautz, L.; Pellecchia, M.; Mustelin, T. Targeting the PTPome in human disease. *Expert Opin. Ther. Targets* **2006**, *10* (1), 157−177.

(8) Julien, S. G.; Dube, N.; Hardy, S.; Tremblay, M. Inside the human cancer tyrosine phosphatome. *Nat. Rev. Cancer* **2011**, *11* (1), 35−49.

(9) Vang, T.; Miletic, A. V.; Arimura, Y.; Tautz, L.; Rickert, R. C.; Mustelin, T. Protein tyrosine phosphatases in autoimmunity. *Annu. Rev. Immunol.* **2008**, *26*, 29−55.

(10) Vintonyak, V. V.; Antonchick, A.; Rauh, D.; Waldmann, H. The therapeutic potential of phosphatase inhibitors. *Curr. Opin. Chem. Biol.* **2009**, *13* (3), 272−283.

(11) Barr, A. J. Protein tyrosine phosphatases as drug targets: strategies and challenges of inhibitor development. *Future Med. Chem.* **2010**, *2* (10), 1563−1576.

(12) He, R.; Zeng, L.; He, Y.; Zhang, S.; Zhang, Z. Small molecule tools for functional interrogation of protein tyrosine phosphatases. *FEBS J.* **2013**, *280*, 731.

(13) Usui, T.; Kojima, S.; Kidokoro, S.; Ueda, K.; Osada, H.; Sodeoka, M. Design and synthesis of a dimeric derivative of RK-682 with increased inhibitory activity against VHR, a dual-specificity ERK phosphatase: implications for the molecular mechanism of the inhibition. *Chem. Biol.* **2001**, *8* (12), 1209−1220.

(14) Sodeoka, M.; Sampe, R.; Kojima, S.; Baba, Y.; Usui, T.; Ueda, K.; Osada, H. Synthesis of a tetronic acid library focused on inhibitors of tyrosine and dual-specificity protein phosphatases and its evaluation regarding VHR and cdc25B inhibition. *J. Med. Chem.* **2001**, *44* (20), 3216−3222.

(15) Ueda, K.; Usui, T.; Nakayama, H.; Ueki, M.; Takio, K.; Ubukata, M.; Osada, H. 4-isoavenaciolide covalently binds and inhibits VHR, a dual-specificity phosphatase. *FEBS Lett.* **2002**, *525* (1−3), 48−52.

(16) Shi, Z.; Tabassum, S.; Jiang, W.; Zhang, J.; Mathur, S.; Wu, J.; Shi, Y. Identification of a potent inhibitor of human dual-specific phosphatase, VHR, from computer-aided and NMR-based screening to cellular effects. *ChemBioChem* **2007**, *8* (17), 2092−2099.

(17) Park, H.; Jung, S.; Jeong, D.; Ryu, S.; Kim, S. Discovery of VHR phosphatase inhibitors with micromolar activity based on structure-based virtual screening. *ChemMedChem* **2008**, *3* (6), 877−880.

(18) Wu, S.; Vossius, S.; Rahmouni, S.; Miletic, A. V.; Vang, T.; Vazquez-Rodriguez, J.; Cerignoli, F.; Arimura, Y.; Williams, S.; Hayes, T.; et al. Multidentate small-molecule inhibitors of vaccinia H1-related (VHR) phosphatase decrease proliferation of cervix cancer cells. *J. Med. Chem.* **2009**, *52* (21), 6716−6723.

(19) Hirai, G.; Tsuchiya, A.; Koyama, Y.; Otani, Y.; Oonuma, K.; Dodo, K.; Simizu, S.; Osada, H.; Sodeoka, M. Development of a Vaccinia H1-related (VHR) phosphatase inhibitor with a nonacidic phosphate-mimicking core structure. *ChemMedChem* **2011**, *6* (4), 617−622.

(20) Rees, D. C.; Congreve, M.; Murray, C. W.; Carr, R. Fragment-based lead discovery. *Nat. Rev. Drug Discovery* **2004**, *3* (8), 660−672.

(21) Hajduk, P. J.; Greer, J. A decade of fragment-based drug design: strategic advances and lessons learned. *Nat. Rev. Drug Discovery* **2007**, *6* (3), 211−219.

(22) Jhoti, H.; Williams, G.; Rees, D. C.; Murray, C. W. The 'rule of three' for fragment-based drug discovery: where are we now? *Nat. Rev. Drug Discovery* **2013**, *12* (8), 644−645.

(23) Hann, M. M.; Leach, A. R.; Harper, G. Molecular complexity and its impact on the probability of finding leads for drug discovery. *J. Chem. Inf. Comput. Sci.* **2001**, *41* (3), 856−864.

(24) Hopkins, A. L.; Groom, C.; Alex, A. Ligand efficiency: a useful metric for lead selection. *Drug Discovery Today* **2004**, *9* (10), 430−431.

(25) Kuntz, I. D.; Chen, K.; Sharp, K. A.; Kollman, P. A. The maximal affinity of ligands. *Proc. Natl. Acad. Sci. U.S.A.* **1999**, *96* (18), 9997−10002.

(26) Maveyraud, L.; Mourey, L. Protein X-ray Crystallography and Drug Discovery. *Molecules* **2020**, *25* (51030.

(27) Oprea, T. I.; Davis, A. M.; Teague, S. J.; Leeson, P. D. Is there a difference between leads and drugs? A historical perspective. *J. Chem. Inf. Comput. Sci.* **2001**, *41* (5), 1308−1315.

(28) Walsh, L.; Erlanson, D. A.; de Esch, I. J. P.; Jahnke, W.; Woodhead, A.; Wren, E. Fragment-to-Lead Medicinal Chemistry Publications in 2021. *J. Med. Chem.* **2023**, *66* (2), 1137−1156.

(29) Ludlow, R. F.; Verdonk, M. L.; Saini, H. K.; Tickle, I. J.; Jhoti, H. Detection of secondary binding sites in proteins using fragment screening. *Proc. Natl. Acad. Sci. U.S.A.* **2015**, *112* (52), 15910−15915.

(30) Pellecchia, M.; Sem, D. S.; Wuthrich, K. NMR in drug discovery. *Nat. Rev. Drug Discovery* **2002**, *1* (3), 211−219.

(31) Jahnke, W. Perspectives of biomolecular NMR in drug discovery: the blessing and curse of versatility. *J. Biomol. NMR* **2007**, *39* (2), 87−90.

(32) Stockman, B. J.; Dalvit, C. NMR screening techniques in drug discovery and drug design. *Prog. Nucl. Magn. Reson. Spectrosc.* **2002**, *41* (3), 187−231.

(33) Pellecchia, M.; Bertini, I.; Cowburn, D.; Dalvit, C.; Giralt, E.; Jahnke, W.; James, T. L.; Homans, S. W.; Kessler, H.; Luchinat, C.; et al. Perspectives on NMR in drug discovery: a technique comes of age. *Nat. Rev. Drug Discovery* **2008**, *7* (9), 738−745.

(34) Blundell, T. L.; Jhoti, H.; Abell, C. High-throughput crystallography for lead discovery in drug design. *Nat. Rev. Drug Discovery* **2002**, *1* (1), 45−54.

(35) Patel, D.; Bauman, J. D.; Arnold, E. Advantages of crystallographic fragment screening: functional and mechanistic insights from a powerful platform for efficient drug discovery. *Prog. Biophys. Mol. Biol.* **2014**, *116* (2−3), 92−100.

(36) Krojer, T.; Fraser, J. S.; von Delft, F. Discovery of allosteric binding sites by crystallographic fragment screening. *Curr. Opin. Struct. Biol.* **2020**, *65*, 209−216.

(37) Dalvit, C.; Vulpetti, A. Ligand-Based Fluorine NMR Screening: Principles and Applications in Drug Discovery Projects. *J. Med. Chem.* **2019**, *62* (5), 2218−2244.

(38) Dalvit, C.; Ardini, E.; Flocco, M.; Fogliatto, G. P.; Mongelli, N.; Veronesi, M. A general NMR method for rapid, efficient, and reliable biochemical screening. *J. Am. Chem. Soc.* **2003**, *125* (47), 14620−14625.

(39) Baranowski, M. R.; Wu, J.; Han, Y. N.; Lambert, L. J.; Cosford, N. D. P.; Tautz, L. Protein Tyrosine Phosphatase Biochemical Inhibition Assays. *Bio-Protoc.* **2022**, *12* (18), No. e4510.

(40) Chen, L.; Wu, L.; Otaka, A.; Smyth, M.; Roller, P.; Burke, T. J.; den Hertog, J.; Zhang, Z. Why is phosphonodifluoromethyl phenylalanine a more potent inhibitory moiety than phosphono-methyl phenylalanine toward protein-tyrosine phosphatases? *Biochem. Biophys. Res. Commun.* **1995**, *216* (3), 976−984.

(41) Groves, M. R.; Yao, Z.; Roller, P.; Burke, T. J.; Barford, D. Structural basis for inhibition of the protein tyrosine phosphatase 1B by phosphotyrosine peptide mimetics. *Biochemistry* **1998**, *37* (51), 17773−17783.

(42) Wagner, S.; Accorsi, M.; Rademann, J. Benzyl Mono-P-Fluorophosphonate and Benzyl Penta-P-Fluorophosphate Anions Are Physiologically Stable Phosphotyrosine Mimetics and Inhibitors of Protein Tyrosine Phosphatases. *Chem. − Eur. J.* **2017**, *23* (61), 15387−15395.

(43) Liu, M.; Mirza, A.; McAndrew, P. C.; Thapaliya, A.; Pierrat, O. A.; Stubbs, M.; Hahner, T.; Chessum, N. E. A.; Innocenti, P.; Caldwell, J.; et al. Determination of Ligand-Binding Affinity (K(d)) Using Transverse Relaxation Rate (R(2)) in the Ligand-Observed (1) H NMR Experiment and Applications to Fragment-Based Drug Discovery. *J. Med. Chem.* **2023**, *66* (15), 10617−10627.

(44) Dubois, B. W.; Evers, A. S. Fluorine-19 NMR spin-spin relaxation (T2) method for characterizing volatile anesthetic binding to proteins. Analysis of isoflurane binding to serum albumin. *Biochemistry* **1992**, *31* (31), 7069−7076.

(45) *Enamine Fluorinated Fragment Library*. https://enamine.net/compound-libraries/fragment-libraries/fluorinated-fragment-library (accessed 2023).

(46) Atxabal, U.; Fernandez, A.; Moure, M. J.; Sobczak, K.; Nycholat, C.; Almeida-Marrero, V.; Oyenarte, I.; Paulson, J. C.; de la Escosura, A.; Torres, T.; et al. Quantifying Siglec-sialylated ligand interactions: a versatile (19)F-T(2) CPMG filtered competitive NMR displacement assay. *Chem. Sci.* **2024**, *15* (27), 10612−10624.

(47) Tautz, L.; Critton, D. A.; Grotegut, S.Protein tyrosine phosphatases: structure, function, and implication in human disease. In *Methods in Molecular Biology*; Humana Press, 2013; Vol. *1053*, pp 179−221 .

(48) Rogers, D.; Hahn, M. Extended-connectivity fingerprints. *J. Chem. Inf. Model.* **2010**, *50* (5), 742−754.

(49) Willett, P. Similarity-based virtual screening using 2D fingerprints. *Drug Discovery Today* **2006**, *11* (23−24), 1046−1053.

(50) Yuvaniyama, J.; Denu, J.; Dixon, J.; Saper, M. Crystal structure of the dual specificity protein phosphatase VHR. *Science* **1996**, *272* (5266), 1328−1331.

(51) Schumacher, M. A.; Todd, J.; Rice, A.; Tanner, K.; Denu, J. Structural basis for the recognition of a bisphosphorylated MAP kinase peptide by human VHR protein Phosphatase. *Biochemistry* **2002**, *41* (9), 3009−3017.

(52) Ruddraraju, K. V.; Aggarwal, D.; Niu, C.; Baker, E. A.; Zhang, R. Y.; Wu, L.; Zhang, Z. Y. Highly Potent and Selective N-Aryl Oxamic Acid-Based Inhibitors for Mycobacterium tuberculosis Protein Tyrosine Phosphatase B. *J. Med. Chem.* **2020**, *63* (17), 9212−9227.

(53) Andersen, H. S.; Iversen, L. F.; Jeppesen, C. B.; Branner, S.; Norris, K.; Rasmussen, H. B.; M?ller, K. B.; M?ller, N. P. 2-(oxalylamino)-benzoic acid is a general, competitive inhibitor of protein-tyrosine phosphatases. *J. Biol. Chem.* **2000**, *275* (10), 7101−7108.

(54) Szczepankiewicz, B. G.; Liu, G.; Hajduk, P. J.; Abad-Zapatero, C.; Pei, Z.; Xin, Z.; Lubben, T. H.; Trevillyan, J. M.; Stashko, M. A.; Ballaron, S. J.; et al. Discovery of a potent, selective protein tyrosine phosphatase 1B inhibitor using a linked-fragment strategy. *J. Am. Chem. Soc.* **2003**, *125* (14), 4087−4096.

(55) Zdrazil, B.; Felix, E.; Hunter, F.; Manners, E. J.; Blackshaw, J.; Corbett, S.; de Veij, M.; Ioannidis, H.; Lopez, D. M.; Mosquera, J. F.; et al. The ChEMBL Database in 2023: a drug discovery platform spanning multiple bioactivity data types and time periods. *Nucleic Acids Res.* **2024**, *52* (D1), D1180−D1192.

(56) Gilson, M. K.; Liu, T.; Baitaluk, M.; Nicola, G.; Hwang, L.; Chong, J. BindingDB in 2015: A public database for medicinal chemistry, computational chemistry and systems pharmacology. *Nucleic Acids Res.* **2016**, *44* (D1), D1045−1053.

(57) Bollag, G.; Tsai, J.; Zhang, J.; Zhang, C.; Ibrahim, P.; Nolop, K.; Hirth, P. Vemurafenib: the first drug approved for BRAF-mutant cancer. *Nat. Rev. Drug Discovery* **2012**, *11* (11), 873−886.

(58) Witham, J.; Valenti, M. R.; De-Haven-Brandon, A. K.; Vidot, S.; Eccles, S. A.; Kaye, S. B.; Richardson, A. The Bcl-2/Bcl-XL family inhibitor ABT-737 sensitizes ovarian cancer cells to carboplatin. *Clin. Cancer Res.* **2007**, *13* (23), 7191−7198.

(59) Park, C. M.; Bruncko, M.; Adickes, J.; Bauch, J.; Ding, H.; Kunzer, A.; Marsh, K. C.; Nimmer, P.; Shoemaker, A. R.; Song, X.; et al. Discovery of an orally bioavailable small molecule inhibitor of prosurvival B-cell lymphoma 2 proteins. *J. Med. Chem.* **2008**, *51* (21), 6902−6915.

(60) de Castro, G. V.; Ciulli, A. Spy vs. spy: selecting the best reporter for (19)F NMR competition experiments. *Chem. Commun.* **2019**, *55* (10), 1482−1485.

(61) Békés, M.; Langley, D. R.; Crews, C. M. PROTAC targeted protein degraders: the past is prologue. *Nat. Rev. Drug Discovery* **2022**, *21* (3), 181−200.

(62) Buckley, D. L.; Crews, C. M. Small-molecule control of intracellular protein levels through modulation of the ubiquitin proteasome system. *Angew. Chem., Int. Ed.* **2014**, *53* (9), 2312−2330.

(63) Hughes, S. J.; Ciulli, A. Molecular recognition of ternary complexes: a new dimension in the structure-guided design of chemical degraders. *Essays Biochem.* **2017**, *61* (5), 505−516.

(64) Rudd, K. E.; Johnson, S. C.; Agesa, K. M.; Shackelford, K. A.; Tsoi, D.; Kievlan, D. R.; Colombara, D. V.; Ikuta, K. S.; Kissoon, N.; Finfer, S.; et al. Global, regional, and national sepsis incidence and mortality, 1990−2017: analysis for the Global Burden of Disease Study. *Lancet* **2020**, *395* (10219), 200−211.

(65) Lambert, L. J.; Grotegut, S.; Celeridad, M.; Gosalia, P.; Backer, L. J.; Bobkov, A. A.; Salaniwal, S.; Chung, T. D.; Zeng, F. Y.; Pass, I.; et al.. Development of a Robust High-Throughput Screening Platform for Inhibitors of the Striatal-Enriched Tyrosine Phosphatase (STEP). *Int. J. Mol. Sci.* **2021**, *22* (94417).

(66) Winn, M. D.; Ballard, C. C.; Cowtan, K. D.; Dodson, E. J.; Emsley, P.; Evans, P. R.; Keegan, R. M.; Krissinel, E. B.; Leslie, A. G.; McCoy, A.; et al. Overview of the CCP4 suite and current developments. *Acta Crystallogr., Sect. D: Biol. Crystallogr.* **2011**, *67* (Pt 4), 235−242.

(67) Vonrhein, C.; Flensburg, C.; Keller, P.; Sharff, A.; Smart, O.; Paciorek, W.; Womack, T.; Bricogne, G. Data processing and analysis with the autoPROC toolbox. *Acta Crystallogr., Sect. D: Biol. Crystallogr.* **2011**, *67* (Pt 4), 293−302.

(68) Murshudov, G. N.; Skubák, P.; Lebedev, A. A.; Pannu, N. S.; Steiner, R. A.; Nicholls, R. A.; Winn, M. D.; Long, F.; Vagin, A. A. REFMAC5 for the refinement of macromolecular crystal structures. *Acta Crystallogr., Sect. D: Biol. Crystallogr.* **2011**, *67* (Pt 4), 355−367.

(69) Liebschner, D.; Afonine, P. V.; Baker, M. L.; Bunkoczi, G.; Chen, V. B.; Croll, T. I.; Hintze, B.; Hung, L. W.; Jain, S.; McCoy, A. J.; et al. Macromolecular structure determination using X-rays, neutrons and electrons: recent developments in Phenix. *Acta Crystallogr., Sect. D: Struct. Biol.* **2019**, *75* (Pt 10), 861−877.

(70) Emsley, P.; Lohkamp, B.; Scott, W. G.; Cowtan, K. Features and development of Coot. *Acta Crystallogr., Sect. D: Biol. Crystallogr.* **2010**, *66* (Pt 4), 486−501.

(71) Chen, V. B.; Arendall, W. B., 3rd; Headd, J. J.; Keedy, D. A.; Immormino, R. M.; Kapral, G. J.; Murray, L. W.; Richardson, J. S.; Richardson, D. C. MolProbity: all-atom structure validation for macromolecular crystallography. *Acta Crystallogr., Sect. D: Biol. Crystallogr.* **2010**, *66* (Pt 1), 12−21.